Research Square

Preprints are preliminary reports that have not undergone peer review.
They should not be considered conclusive, used to inform clinical practice,
or referenced by the media as validated information.

Pleural mesothelioma cell-derived sEVs promote epithelial-to-mesenchymal transition and T-cell suppression through the PD-L1 pathway

Sareh Zhand
University of Technology Sydney
Hamidreza Aboulkheyr
University of Technology Sydney
Emma Rath
Victor Chang Cardiac Research Institute
Dale Mark Goss
University of Technology Sydney
Ziyao Cheng
University of Technology Sydney
Julia Shi Hua Ngai
University of Technology Sydney
Ziyu Wang
The University of Sydney
Jiayan Liao
University of Technology Sydney
Olivia Guido
Garvan Institute of Medical Research
Elizabeth Lawfull
Garvan Institute of Medical Research
Xiaofeng Cheng
University of Technology Sydney
Marco A. Enriquez Martinez
University of Queensland
Nicholas J. Wastra van Holthe
University of Queensland
Alan E. Rowan
University of Queensland
Majid Ebrahimi Warkiani
University of Technology Sydney

Yuen Yee Cheng

yuenyee.cheng@uts.edu.au

University of Technology Sydney

Research Article

Keywords: Mesothelioma, Small EV, PD-L1, Epithelial-Mesenchymal Transition, immune escape

Posted Date: September 23rd, 2026

DOI: https://doi.org/10.21203/rs.3.rs-10485987/v1

License: This work is licensed under a Creative Commons Attribution 4.0 International License.
Read Full License

Additional Declarations: No competing interests reported.

Pleural mesothelioma cell-derived sEVs promote epithelial-to-mesenchymal transition and T-cell suppression through the PD-L1 pathway

Sareh Zhand[1,2¥,₸], Hamidreza Aboulkheyr [2¥], Emma M Rath[3,4], Dale Mark Goss[2], Ziyao Cheng[1], Julia Shi Hua Ngai[1], Ziyu Wang[5,6,7], Jiayan Liao[1], Olivia Guido[8], Elizabeth Lawfull[8], Xiaofeng Cheng[1], Marco A. Enriquez Martinez[9], Nicholas J. Wastra van Holthe[10], Alan E. Rowan[10,†], Majid Ebrahimi Warkiani[1,2,#, *], Yuen Yee Cheng[2*]

[1] Institute for Biomedical Materials and Devices, Faculty of Science, University of Technology Sydney, New South Wales 2007, Australia

2 School of Biomedical Engineering, University of Technology Sydney, Sydney, New South Wales 2007, Australia

[3] Giannoulatou Laboratory, Victor Chang Cardiac Research Institute, Darlinghurst, New South Wales, 2010, Australia.

[4] School of Clinical Medicine, Faculty of Medicine and Health, University of New South Wales, Sydney, New South Wales 2052, Australia

[5] Charles Perkin Centre, Sydney, New South Wales 2006, Australia

[6] School of life and Environmental science, University of Sydney, Sydney, New South Wales 2006, Australia

[7] The Baird Institute, Sydney, New South Wales 2042, Australia

[8] Australian BioResources, Moss Vale, New South Wales 2577, Australia

[9] Australian Institute for Bioengineering and Nanotechnology, Institute for Molecular Biosciences (IMB), University of Queensland, Queensland, Australia,

[10] Australian Institute for Bioengineering and Nanotechnology, University of Queensland, Queensland, Australia,

[†] Current affiliation of Alan E. Rowan is University of Wollongong, NSW, Australia

current affiliation of Majid Ebrahimi Warkiani is Advanced Biosciences and Bioengineering Research Center, American University of Sharjah, UEA

₸ current affiliation of Sareh Zhand is Storr Liver Centre, The Westmead Insittute for Medical Research, University of Sydney, Westmead, NSW, Australia

[¥]These authors contributed equally as the first author.

*** Corresponding authors:**

Yuen Yee Cheng (yuenyee.cheng@uts.edu.au)

School of Biomedical Engineering, University of Technology Sydney, Sydney, New South Wales 2007, Australia

Majid Ebrahimi Warkiani (Mwarkiani@aus.edu)

Majid Ebrahimi Warkiani is Advanced Biosciences and Bioengineering Research Center, American University of Sharjah, UEA

Abstract

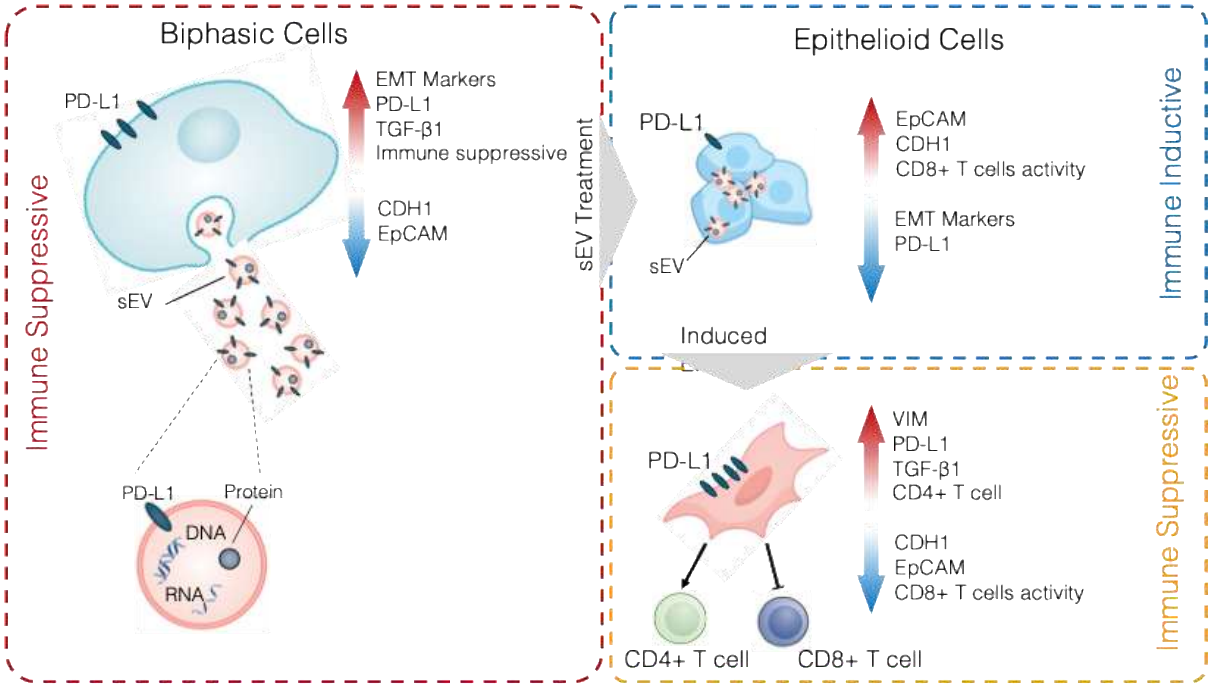
Background
Pleural mesothelioma (PM) is a highly aggressive malignancy with limited durable responses to immune checkpoint blockade, largely due to poorly defined tumour-intrinsic mechanisms of immune evasion. Small extracellular vesicles (sEVs) have emerged as key mediators of tumour progression, yet their role in coordinating phenotypic plasticity and suppressing anti-tumour immunity in PM remains poorly understood.

Methods
Given the central role of epithelial-to-mesenchymal transition (EMT) in tumour aggressiveness, we investigated whether PM cells of the biphasic histologic subtype exploit sEVs to propagate EMT-associated and immunomodulatory signals. sEVs were isolated from human (MSTO-211H, NCI-H28) and murine (AB1, AB22) PM cell lines using differential ultracentrifugation and comprehensively characterized via nanoparticle analysis, immunoblotting, proteomics, and cytokine profiling. A 3D multicellular organoid model incorporating immune cells was used to assess sEV-mediated effects on the tumour immune microenvironment.

Results
Biphasic/mesenchymal PM cells and their sEVs were selectively enriched in TGF-β1 and EMT-related transcriptional regulators. Consistently, exposure of epithelial NCI-H28 and AB22 cells to sEVs from biphasic PM cells induced hallmark EMT features, including reduced EpCAM, increased vimentin expression, and enhanced migration and proliferation, as confirmed by immunofluorescence. Notably, PD-L1 was significantly elevated in biphasic cell-derived sEVs, prompting functional evaluation in a physiologically relevant 3D tumour–immune co-culture system. PD-L1–positive sEVs suppressed $CD8^+$ T-cell proliferation and decreased CD8 expression, demonstrating a direct vesicle-mediated mechanism of immune suppression. Tumour microenvironment profiling of biphasic PM further revealed a stromal-rich and immune-suppressed niche consistent with these effects. These findings establish that biphasic PM-derived sEVs act as drivers of EMT and PD-L1–mediated T-cell inhibition, implicating sEV-associated signalling pathways as promising targets to overcome immunotherapy resistance in pleural mesothelioma.

Conclusions
Biphasic/mesenchymal PM-derived sEVs drive phenotypic transition and immune reprogramming in pleural mesothelioma. Targeting sEV-mediated intercellular communication may represent a novel strategy to enhance immunotherapy efficacy in this disease.

Keywords: Mesothelioma, Small EV, PD-L1, Epithelial-Mesenchymal Transition, immune escape.



Graphical Abstract: Graphical Abstract | Differential immune and EMT programs in mesothelioma subtypes. Biphasic MSTO cells display an immune-suppressive phenotype with elevated EMT markers, PD-L1, and TGF-β1, and release sEVs enriched in PD-L1. These sEVs reinforce EMT and immune suppression by downregulating epithelial adhesion markers (CDH1, EpCAM) and impairing $CD8^+$ T-cell activity. In contrast, epithelioid H28 cells exhibit an immune-inductive phenotype under basal conditions, with high CDH1/EpCAM and enhanced $CD8^+$ T-cell activity. However, exposure to MSTO-derived sEVs induces EMT and immune-suppressive reprogramming in epithelioid cells, characterized by VIM, PD-L1, TGF-β1 upregulation and $CD4^+$ T-cell recruitment. MSTO-sEVs could be known as drivers of EMT plasticity and immune evasion, shifting epithelioid cells toward an immune-suppressive state.

Introduction

Pleural mesothelioma (PM) is an aggressive cancer of lung lining as a result of previous asbestos exposure either occupationally or environmentally. [1] Limited biomarkers and histopathological heterogeneity frequently delay diagnosis, contributing to a median survival of 9–18 months. [2,3] The three main histological subtypes of PM: epithelioid, biphasic, and sarcomatoid, [4] not only differ in morphology but also in prognosis, with biphasic and sarcomatoid subtypes being associated with a worse prognosis.[5] PM development and metastasis have been correlated to epithelial-to-mesenchymal transition (EMT) [6] a reversible cellular programme in which epithelial cells lose adhesion, polarity and basement membrane anchorage while acquiring mesenchymal, migratory and invasive properties, [7,8] resulting in a poor prognosis for the patient. [9] As a central regulator of tumour plasticity, EMT profoundly shapes the PM tumour microenvironment and represents a potential source of diagnostic and therapeutic targets.

Beyond promoting invasion, EMT contributes to immune evasion in PM, partly through upregulation of programmed death-ligand 1 (PD-L1).[10] EMT-driven PD-L1 induction has been demonstrated across multiple malignancies, including lung adenocarcinoma and mesothelioma. [11] PD-L1 engages the PD-1 receptor on T cells to suppress antitumour immunity by inhibiting priming, proliferation and effector function while promoting apoptosis. [12,13] In cancer, tumour cells use the PD-L1/PD1 pathway to escape from T-cell-mediated antitumour responses. PD-L1-overexpressing tumour cells can therefore survive, escape from surveillance by the immune system, and invade adjacent tissue. [13,14] In PM, PD-L1 is frequently expressed at higher levels in biphasic and sarcomatoid subtypes, contributing to clinically aggressiveness, [15-17] poor prognosis and reduced responsiveness to immune checkpoint blockade. [17]

Recent studies have highlighted that extracellular vesicles (EVs) are mediators of EMT-associated signalling within the tumour microenvironment, facilitating intercellular communication. [18] EVs are lipid-bilayer-enclosed particles released from various type of cells such as immune cells, fibroblasts and endothelial cells, into the extracellular space and microenvironment, and are important for intercellular communication and tumour pathogenesis in particular. [19] There are three main classes: small EVs (sEVs, 30-150 nm diameter), microvesicles (100 nm – 1μm), and apoptotic bodies (> 1 μm). While sEVs play an essential role in physiological and pathological processes, including immune response,[20] signal transduction, [21] and tumour initiation, progression, invasion, and metastasis. [22,23] Despite the broad diversity in origin of sEVs, they are all enriched in some common structural and functional proteins, such as tetraspanins family (CD9, CD81, CD82, and CD63), [24] Rab GTPase, *N*-ethylmaleimide-sensitive factor attachment protein receptors (SNAREs), annexins, Alix (protein regulating cellular mechanisms), TSG101 (tumour susceptibility gene 101 protein), MHC1 (major histocompatibility complex 1), and HSP90 (heat shock protein 90). [25] It is known that tumour-derived sEVs can interact with recipient cells via the receptor/ligand type signalling or integrin-mediated adhesion or they can be internalized by endocytosis or phagocytosis. [26] Tumour-derived sEVs contribute to EMT induction by transporting canonical EMT regulators, including TGF-β, IL-6, β-catenin, HIF-1α and EMT-associated microRNAs such as miR-23a, thereby inducing EMT-like phenotypic and functional changes in recipient cells. [27] In parallel, sEVs mediate immune suppression through the transfer of PD-L1. [28 29] *In vitro* and *in vivo* models have shown that PD-L1 can be transferred via sEVs to other cells in a dose-dependent manner. [30] Tumour-derived sEVs-associated PD-L1 has been discussed in different tumour types, including lung, [31] breast, [30] prostate, [32] head and neck, [33,34] oral-esophageal, [35] and gastric cancers. [36] Soluble PD-L1, sEV-bound PD-L1 exhibits enhanced immunosuppressive activity, inducing $CD8^+$ T-cell apoptosis and augmenting regulatory T-cell function. [31] These studies indicated the potential of tumour-derived sEVs -associated PD-L1

has the ability to induce apoptosis in CD8+ T-cells and enhance the suppressing activity of T-regs in a dose-dependent manner. [34]

The mechanistic link between epithelial–mesenchymal plasticity and immune evasion in PM remains poorly understood. In this study, we identify a previously unrecognized pathway through which biphasic/mesenchymal mesothelioma cells transmit aggressive signals to epithelial tumour cells via sEVs. Using both conventional 2D models and multicellular 3D mesothelioma organoids incorporating immune components, we proof our hypothesis that sEVs derived from biphasic/mesenchymal cells promote aggressive phenotypic reprogramming and suppress CD8+ T cells activity, increased expression of the immune checkpoint molecule PD-L1. Proteomic profiling further identifies candidate sEV-associated biomarkers linked to this phenotypic transition. We tested our hypothesis that mesenchymal tumour in PM actively propagate EMT and immune suppression through sEV-mediated communication, suggests by targeting sEV signalling may represent a strategy to sensitize epithelial, immunologically "cold" mesothelioma to immunotherapy.

Materials and methods

Detailed reagents and experimental procedures are provided in the Supplementary Information.

Cell lines

Human mesothelioma cell lines (MSTO-211H, biphasic, and NCI-H28, epithelioid were obtained from ATCC and repeatedly tested negative for mycoplasma by in-house testing at the University of Technology Sydney. AB22 cells (epithelioid), and murine mesothelioma cell lines (AB1, biphasic) were supplied by Cell Bank Australia (Westmead, NSW, Australia) as catalogue number CBA-0144 and CBA-0148. Cells were maintained in RPMI 1640 (Gibco, UK) supplemented with 10% (v/v) fetal calf serum (FCS, Gibco, UK), 100 U/mL penicillin and 100 mg/mL streptomycin (Gibco, UK) in a T25 tissue culture flask (ThermoFisher, USA) and incubated at 37ºC in a 5% CO_2 humidified incubator. Both human and murine models and epithelioid/biphasic subtypes were used to reflect pleural mesothelioma heterogeneity and enable downstream immunological assays in a syngeneic system.

Immunofluorescence staining of humans and murine derived mesothelioma cells for EMT markers.

Vimentin (as a mesenchymal marker), E-Cadherin and EPCAM (as an epithelial marker) were used for immunofluorescence staining. Cells (1×10^4) were plated in 96-well glass-bottom plates, fixed with 4% PFA, permeabilized with 0.1% Triton X-100 in PBS, and blocked in 5% BSA + 3% goat serum. Primary antibodies (anti-EpCAM, anti-E-cadherin, anti-vimentin; 1:100) were incubated overnight at 4 °C following the addition of secondary antibodies (anti-mouse Alexa Fluor 594; anti-rabbit Alexa Fluor 488; 1:200). Imaging was performed by confocal microscopy (Leica Stellaris 5) and quantified by ImageJ software. Similarly, the anti-PD-L1 antibody was used to evaluate the expression of PD-L1 on the surface of the above-mentioned cells.

Small EV isolation from conditioned medium (CM) using ultracentrifugation.

Cell conditioned medium (CM) preparation, MSTO-211H and AB1 cells cultured in T175 flasks at ~70% confluency (approximately 3×10^8 cells) and incubated in sEV-free RPMI-1640 (no FCS) for 48 hours at 37 °C, 5% CO_2, 2% O_2 (hypoxic conditions). Media were collected and sequentially centrifuged at 300×g (10 minutes;19776 rotor, Sigma, USA), 2,000×g (20 minutes;19776 rotor, Sigma, USA), and 10,000×g (30 minutes; Sigma 19776 rotor) and filtered (0.22 µm). sEVs were pelleted by ultracentrifugation at 100,000×g (120 minutes; Beckman F37L Ti), washed in PBS, and ultracentrifuged again at 100,000×g (120 minutes).

Pellets were resuspended in 500 µl 0.22 µm-filtered PBS (WHA9913-2502, Sigma Aldrich, USA) and stored at −80 °C. All steps were done at 4 °C. sEV characterisation—including nanoparticle tracking analysis, western blotting, cryo-electron microscopy, and uptake assays—were performed as described in the Supplementary Information.

Immunofluorescent staining of PM cells for EMT marker expression post sEV treatment.

Human epithelial mesothelioma cells (NCI-H28) were treated with the sEVs derived from human biphasic mesothelioma cells (MSTO-211H), or the EMT-kit (CCM017, R&D systems, USA) as a positive control. In parallel, the murine epithelial mesothelioma cells (AB22) were treated with the sEVs derived from murine biphasic mesothelioma cells (AB1). Due to the lack of a commercially available EMT-inducing kit specific to mouse cells, no control EMT kit was used in the murine experiments. Briefly, the 3×10^5 cells were seeded in a 6 well plate, 10µg/mL of sEV, or EMT-kit were added to the cells post seeding for overnight. The cells were incubated for further 48 hours in 37ºC temperature at 5% CO_2 incubator. The NCI-H28 and AB22 cells with RPMI-1640 medium were used as negative control. For the immunofluorescence staining of the fixed cells the anti-human E-Cadherin antibody and anti-human Vimentin antibody were performed and analysed as described above.

Immunocapture-based ELISA and western blotting method for the detection of PD-L1

Soluble PD-L1 expression in NCI-H28 cells treated with MSTO-211H sEVs or EMT-kit was quantified by human PD-L1 ELISA (ab277712) according to the manufacturer's protocol. For western blotting, [37] cells were lysed in RIPA buffer after 48 hours, clarified (2,000×g, 5 minutes, 4 °C), quantified by BCA, and 10 µg protein was resolved by SDS–PAGE and transferred to PVDF. Membranes were blocked (5% milk, 30 minutes) and probed overnight at 4 °C with PD-L1 and vimentin (1:1,000 in PBS-T), followed by HRP-conjugated secondary antibodies (1:20,000; 2 hours). Detection used SuperSignal West Dura. PD-L1 and vimentin were resolved under reducing/denaturing conditions.

Cytokine array

For cytokine array testing, the human cytokine antibody array (ab133996, Abcam, USA) was performed on the NCI-H28 cells treated with MSTO-211H-derived sEVs, with the EMT-kit as a positive control, and MSTO-211H derived sEVs. Briefly, the 3×10^5 NCI-H28 cells were seeded in 6 well plate and after 24 hours, the concentration of 10µg of sEV derived from MSTO-211H cells, and the proper amount of EMT-kit were added to the NCI-H-28 cells as control. The cells were incubated for further 48 hours in 37ºC temperature at 5% CO_2 incubator. The NCI-H28 cells with RPMI-1640 medium was used as a negative control. After 48 hours the conditioned medium was collected and used for the cytokine array test according to manufacturer's protocol. The membranes were imaged in Amersham Imager 600 system (AI 600, Vanderbilt Brain Institute, US).

Analysis of TGF-β Secretion

NCI-H28 human mesothelioma cells and AB22 murine mesothelioma cells were seeded in 6-well plates. NCI-H28 cells were treated with 10µg MSTO-211H derived-sEVs, MSTO cell derived conditioned medium depleted of sEVs (CM-no-sEV), or left untreated as controls. In parallel, AB22 cells were treated with similar concentration of AB1-derived sEVs, AB1 cell conditioned medium depleted of sEVs, or left untreated. Treatments were carried out in RPMI containing 10% FBS for 48 hours. Supernatant was subsequently collected for further analysis. TGF-β levels in conditioned media were quantified using Human/Mouse TGF beta 1 Uncoated ELISA Kit (# 88-8350, Invitrogen, Australia) according to the manufacturer's instructions. RPMI supplemented with 10% FBS incubated under identical conditions in the absence of cells was included as a media-only control to account for serum-derived background, and values

obtained from this control were subtracted from all samples. TGF-β concentrations were normalized to total cellular protein content measured from matched cell lysates collected at the time of supernatant harvest.

Immunoblot Analysis of SMAD2/3 Signalling

Using the same experimental conditions described above, cells were harvested 4 hours post treatment for analysis of SMAD pathway activation. Cells were lysed in RIPA buffer supplemented with protease and phosphatase inhibitors. 20 µg of protein were resolved by SDS–PAGE and transferred to PVDF membranes. Membranes were probed with 1:800 phospho-SMAD2/SMAD3 (Ser465/467, Ser423/425) polyclonal antibody (#PA5-110155, ThermoFisher, Australia) in 5% Skimmed milk, followed by 1:2000 Goat anti-Rabbit HRP-conjugated secondary antibody in PBST. Immunoreactive bands were detected by enhanced chemiluminescence, and phospho-SMAD2/3 signals were normalized to GAPDH to control protein loading.

Proliferation Assay

NCI-H28 cells (2,500 cells) were seeded in 96-well plates, sEVs derived from MSTO-211H cells (10 µg) were added to cells the following day. The untreated cells served as a negative control. The cells were incubated with the treatment for 72 hours. Following treatment, Alamar Blue reagent (Thermo Fisher Scientific) was used for cell proliferation analysis according to manufacturer's protocol. Absorbance was measured using a microplate reader (BioTek Instruments, Winooski, VT, USA) at an excitation wavelength of 570 nm and an emission wavelength of 585 nm. Cell proliferation was quantified by comparing the intensity of treated cells to that of the untreated control cells. All experiments were performed in triplicate, and data were presented as mean ± standard deviation. Statistical analysis was conducted using Student's T-test, with a p-value < 0.05 considered statistically significant.

Migration Assay

NCI-H28 cells (2,500 cells) were seeded in 96-well glass bottom plates and after seeding overnight, cells were labelled with CellTracker Green CMFDA Dye (Thermo Fisher Scientific) according to the manufacturer's instructions. After CellTracker incubation, cell will be treated with MSTO-derived sEVs (10 µg), EMT kit as positive control, untreated cells were used as negative control. Migration of cells was monitored using a live-cell imaging system (Nikon Eclipse Ti-S, Nikon Instruments, Tokyo, Japan) equipped with a temperature and CO_2 control chamber. Images were captured at 0 hours and every 30 minutes for a total of 24 hours. The migration of individual cells was manually tracked using ImageJ to record the coordinates for each cell at each time point. For further analysis of migratory behaviour, including total distance, and maximum distance travelled, the origin plots were utilized.

Cell Cycle Analysis

NCI-H28 cells were divided into three groups: untreated control (H28), EMT-induced (H28 EMT), and MSTO-211H derived sEV-treated (H28 MSTO EV 10ug). Cells were incubated with the above-mentioned treatments for a further 48 hours. Cells were harvested, fixed in 70% ethanol at -20°C overnight and resuspended in a staining solution containing 50 µg/mL propidium iodide (PI; Sigma-Aldrich) and 100 µg/mL RNase A (Thermo Fisher Scientific) in PBS. Samples were incubated at 37°C for 30 minutes in the dark and analysed using a CytoFLEX LX, Beckman Coulter, USA flow cytometer. Data was analysed using CytExpert software 2.4 to determine the percentage of cells in Sub-G1, G0/G1, S, and G2/M phases.

Analysis of $CD4^+$ and $CD8^+$ T Cells expression in 2D platform

Balb/c mice splenocytes were harvested and processed to isolate immune cells including T cells. T cell activation was performed using anti-mouse CD3-coated plates (1µg/mL, 16-0032-82 eBioscience, Invitrogen), followed by co-stimulation with anti-mouse-CD28 antibody (5µg/mL, 16-0281-82 eBioscience, Invitrogen) and supplementation with interleukin-2 (IL-2), which gradually increased from 20 U/mL to 200 U/mL over five days.

After T cell activation, 10 µg of sEVs isolated from AB1 mesothelioma cells (Balb/c-derived) were added to previously cultured AB22 epithelioid mesothelioma cells (Balb/c-derived) in a 6-well plate. A control group without sEVs treatment was included to prevent nonspecific T cell activation. Co-cultures were incubated for two days at 37°C and 5% CO_2. After two days, the supernatant was collected for flow cytometry analysis using PerCP-Cy5.5-conjugated rat anti-mouse CD8a (clone 53-6.7, BD Pharmingen, Australia) and Brilliant Violet 785™ anti-mouse CD4 (100453, BioLegend, Australia). Flow cytometry data acquisition was performed using CytoFLEX LX, Beckman Coulter, USA. The histogram was drawn using CytExpert software 2.4.

Analysis of $CD4^+$ and $CD8^+$ T Cell Expression in 3D platform

Activated T cells were co-cultured with AB22 murine mesothelioma cells in a three-dimensional matrix composed of type I collagen and polyisocyanopeptide (PIC) hydrogel [38,39]. PIC polymer with a viscosity average molecular weight (Mv) of 272kg/mol was prepared by polyerising isocyanide monomer 2-(2-(2-methoxyethoxy)ethoxy)ethyl((R)-2 isocyanopropanoyl)-L-alaninate with nickel catalyst as previously described. [39] 3D organoids were prepared by using a collagen type I stock solution from bovine skin (2.9-3.2 mg/mL; C4243-100ML, Sigma) neutralized on ice with 10X PBS (Gibco) and 7.5% Na2HCO3 to pH 7.4. A final mixture of collagen (2mg/ml) and PIC (low molecular weight, 0.2 mg/ml) hydrogel was prepared and kept on ice. Cells were embedded at a density of 5×10^6 cells/mL, consisting of a 1:1 ratio of activated T cells and AB22 cells, into the Millicell-HA 0.45 µm culture inserts (12 mm diameter) (N1NMA1J32, MILLIPOER) and transferred into 24-well plates. Gels were allowed to polymerize for 30 minutes at 37°C before adding 500 µL of RPMI-1640 complete medium. To investigate the immunomodulatory effect of sEVs, 10µg of purified sEVs derived from AB1 mesothelioma cells, were added to the culture medium immediately following gel polymerization. After 48 hours of co-culture, 3D samples were fixed in 4% paraformaldehyde (PFA; Sigma-Aldrich), processed through a graded ethanol series using an Excelsior AS tissue processor (Bio-Strategy, Australia), cleared with xylene, and embedded in paraffin using a Histostar tissue embedding system (Thermo Fisher Scientific). Paraffin-embedded gels were sectioned at 5 µm thickness using an Epredia Microm HM325 microtome and mounted on Trajan slides series 2 enhanced adhesive (Trajan Scientific, Australia). Sections were deparaffinized and blocked in blocking buffer (PBS containing 5% FBS and 0.3% Triton X-100) in a humidified chamber. Primary antibodies against mouse CD8α (clone 53-6.7) and CD4 (clone GK1.5) (BioLegend; 1:100) were applied to sections in antibody dilution buffer (PBS, 1% BSA, 0.3% Triton X-100). After PBS washes, sections were incubated with Alexa Fluor 488- or 594-conjugated secondary antibodies (1:500; Invitrogen). Nuclei were counterstained with DAPI (1 µg ml^{-1}), mounted with ProLong Gold Antifade Mountant (Invitrogen), and imaged using a Leica Stellaris confocal microscope. $CD8^+$ and $CD4^+$ T cells were quantified by counting positive cells in five randomly selected high-power fields (40×) per section using ImageJ.

Hematoxylin and Eosin (H&E) Staining

Paraffin sections were deparaffinized in xylene and rehydrated through a descending ethanol series (100%, 95%, 70%) followed by rinsing in distilled water. Hematoxylin (Mayer's, Sigma-Aldrich) was applied to stain nuclei, followed by eosin Y solution (Sigma-Aldrich) to stain the

cytoplasm. Stained slides were examined under a light microscope (Olympus BX53) 40× magnification using a DP74 camera and CellSens software. Morphological features such as nuclear condensation, cell detachment, and lymphocyte infiltration were assessed and annotated manually.

Cytokine Profiling in AB22–T cells Co-cultures Treated with AB1-Derived sEVs

Cytokine secretion from co-cultures was assessed using the AB22–T cells co-culture setup described above, with or without the addition of 10 µg of AB1-derived sEVs. Following 48 hours of incubation, the culture supernatants were harvested and analysed using the Proteome Profiler Mouse Cytokine Array Kit, Panel A (ARY006, R&D Systems) according to the manufacturer's instructions. Briefly, membranes pre-spotted with duplicate cytokine capture antibodies were blocked and incubated with 1 mL of conditioned media pre-mixed with a biotinylated detection antibody cocktail. After washing, membranes were incubated with streptavidin–HRP and developed using enhanced chemiluminescence. Blots were imaged using a Bio-Rad ChemiDoc system. Densitometric analysis was performed in ImageJ (Fiji). All intensities were normalized to internal reference spots present on each membrane.

Liquid Chromatography–Tandem Mass Spectrometry (LC–MS/MS)

Proteins from cells and sEVs were processed using an adapted STAGE Tip–based workflow and analysed by nanoLC–MS/MS on a Q Exactive Plus mass spectrometer using data-dependent acquisition. Resulting spectra were searched against the human proteome with stringent false discovery rate control, and pathway-level changes were assessed by gene set enrichment analysis. Detailed descriptions of the LC–MS/MS workflow, data processing, and gene set enrichment analyses are provided in the Supplementary Information.

Results

Biphasic mesothelioma exhibits an immunosuppressive tumour microenvironment linked to EMT

To define subtype-specific tumour microenvironment (TME), we analysed data from The Cancer Genome Atlas (TCGA) pleural mesothelioma (n = 80; Fig. 1). Epithelial tumours were enriched in epithelioid cells, whereas biphasic tumours contained higher proportions of endothelial and mesenchymal cells, consistent with a stroma-rich TME (Fig. 1 A). Immune deconvolution showed higher $CD8^+$ T-cell fractions in epithelioid tumours and increased $CD4^+$ T cells in biphasic tumours (Fig. 1 A). Stromal and immune score analyses demonstrated a negative association between the two compartments, with biphasic tumours exhibiting elevated stromal scores but reduced immune scores, indicating an immunosuppressive microenvironment (Fig. 1 B, C). Cell-type abundance analysis further confirmed higher $CD8^+$ T-cell infiltration in epithelioid tumours (Fig. 1 D), whereas biphasic tumours showed increased regulatory T-cell (Treg)(Fig. 1 E) and significantly higher expression of immunosuppressive genes, including CD274 (PD-L1), CD276, PVR, TGFB1 and NT5E (Fig. 1 F; calculated as GSVA score), supporting a "cold" tumour immune microenvironment (TIME) characterised by low $CD8^+$ infiltration, elevated Tregs and a stromal-driven immunosuppressive phenotype. EMT-related genes expression indicated biphasic tumours expressed elevated levels of canonical EMT genes (CDH2, VIM, AXL, TGFB1, ZEB1), whereas epithelial markers (CDH1, EPCAM, CLDN7) were more abundant in epithelioid tumours (Fig. 1G). Additionally, EMT scores were significantly higher in biphasic tumours (>1.2) compared to epithelioid (<1.2) (Fig. 1 H), and the high mesenchymal gene expression correlated with reduced overall survival (OS) (Fig. 1 I). Correlation analysis between EMT genes and immune activities revealed a positive association between low or suppressed

immune cells activity and expression of mesenchymal-related genes (Fig. 1 J). Immune cell populations revealed enrichment of cytotoxic T cells in epithelial-like tumours, while biphasic/mesenchymal-like tumours showed increased Treg proportions (Fig. 1 K). Consistent with an immunosuppressive TME, mesenchymal-enriched samples expressed higher levels of immune checkpoints PD-L1 (CD274), PD-1 (PDCD1) and CTLA4, as well as the Treg marker FOXP3 (Fig. 1 L, M). Correlation analysis confirmed strong negative associations between mesenchymal markers (CDH2, VIM) and cytotoxic T-cell infiltration, whereas epithelial CDH1 showed a positive correlation (Fig. 1 N). VIM expression aligned with higher PD-L1 and FOXP3 expression (Fig. 1 N), reinforcing the link between EMT and immune suppression.

To model EMT-associated immune modulation in vitro, analysis of nine mesothelioma cell lines (Fig. 1 O) identified NCI-H28 as an epithelial-like cell line with high EPCAM, low VIM (Fig. 1 P) and low PD-L1 expression (Fig. 1 Q), whereas MSTO-211H displayed a mesenchymal phenotype with high VIM, high PD-L1 (Fig. 1 Q) and strong VIM–PD-L1 correlation. We therefore hypothesis that MSTO-211H-derived sEVs express PD-L1 and could reprogramme epithelial-like cells toward EMT. Transcriptomic profiling of murine AB1 and AB22 mesothelioma models showed that AB1 cells exhibit markedly higher expression of mesenchymal markers (TGF-β1, MMP14, CDH2, ZEB2, SNAI2, VIM) and PD-L1 relative to AB22 (Fig. 1 R), with hierarchical clustering separating the two cell lines by EMT- and immune-related genes. GSEA indicated upregulation of hallmark EMT, inflammatory response, allograft rejection and G2/M checkpoint pathways (Fig. 1 S). Comparative dot plots confirmed increased PD-L1 in AB1 (Fig. 1 T). TGF-β1 expression was significantly elevated in AB1 ($p < 0.0001$) (Fig. 1 U), which consistent with a mesenchymal-like and immunosuppressive transcriptional phenotype.

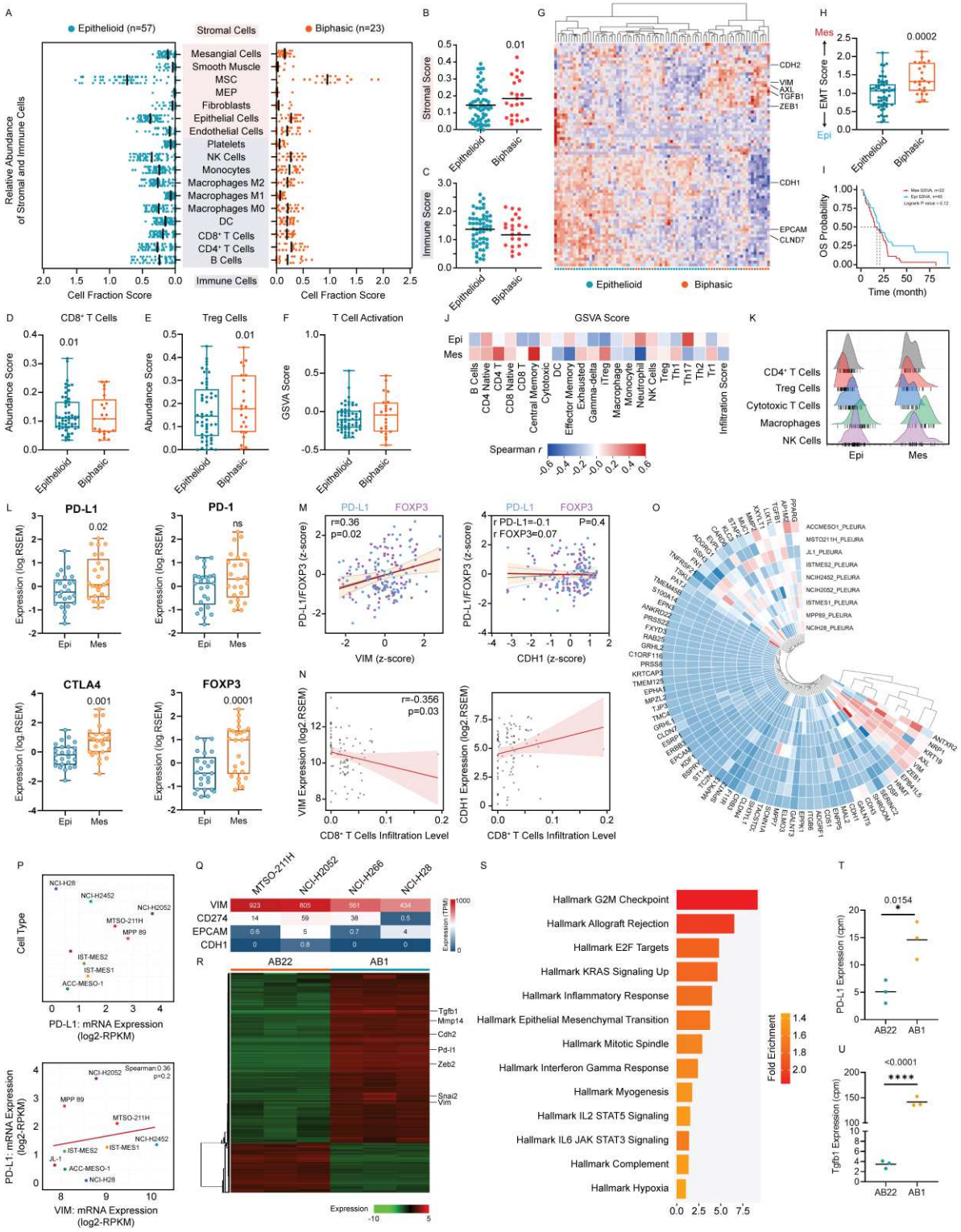


Figure-1: Tumour microenvironment composition, EMT features, and immune modulation in mesothelioma subtypes. (A) Relative abundance of stromal and immune cell fractions in epithelioid (n = 57) and biphasic (n = 23) tumours, showing distinct tumour microenvironment (TME) compositions. (B–C) Stromal and immune scores demonstrate higher stromal content and reduced immune activity in biphasic tumours. (D–E) Abundance of CD8⁺ T cells (D) and regulatory T cells (Tregs, E), with biphasic tumours characterized by reduced CD8⁺ infiltration and enrichment of Tregs. (F) Gene set variation analysis (GSVA) of immune checkpoint activity reveals increased immunosuppressive signaling in biphasic tumours. (G) Heatmap comparing expression of epithelial (CDH1, EpCAM, CLDN7) and mesenchymal (VIM, AXL,

TGFB1, ZEB1, CDH2) markers across mesothelioma cell lines, highlighting subtype-specific EMT programs. (H) EMT scores show significantly higher EMT activity in biphasic cases. (I) Kaplan–Meier analysis of overall survival stratified by epithelial versus mesenchymal GSVA signatures indicates a trend towards poorer survival in mesenchymal-enriched tumours. (J) Correlation matrix of epithelial and mesenchymal GSVA scores with immune subsets highlights differential associations of EMT status with immune infiltration. (K) Distribution of $CD4^+$ T cells, cytotoxic T cells, Tregs, macrophages, and NK cells across epithelial- versus mesenchymal-like tumours. (L) Expression of immune checkpoint genes (PD-L1, PD-1, CTLA4, FOXP3) across subtypes, showing increased checkpoint activity in mesenchymal tumours. (M) Relationship between PD-L1/FOXP3 ratio and EMT status, indicating EMT-associated modulation of the immunosuppressive microenvironment. (N) Negative correlation between EMT markers (VIM, CDH1) and $CD8^+$ T-cell infiltration. (O) Heatmap of canonical EMT gene expression across nine human mesothelioma cell lines, highlighting variable epithelial and mesenchymal transcriptional signatures. (P) Correlation between PD-L1 expression and VIM transcript levels, suggesting EMT-associated upregulation of PD-L1. PD-L1 mRNA expression (log_2-RPKM) across multiple mesothelioma cell lines, indicating variable immune checkpoint regulation. (Q) Expression levels (TPM) of selected EMT and immune checkpoint genes (VIM, CD274/PD-L1, EpCAM, CDH1) across representative cell lines, showing strong mesenchymal bias in biphasic MSTO-211H versus epithelial NCI-H28. (R) Heatmap of EMT and immune-regulatory genes in AB22 versus AB1, demonstrating enrichment of TGF-β1, PD-L1, VIM, and EMT transcription factors (ZEB2, SNAI2) in the biphasic subtype. (S) Gene set enrichment analysis (GSEA) in mesenchymal-like cell lines demonstrates enrichment of proliferative and inflammatory pathways, including G2M checkpoint, KRAS signalling, interferon-γ response, and EMT. (T) Comparison of PD-L1 expression (cpm) between biphasic AB1 and epithelioid AB22, showing significantly higher expression in AB1. (U) Expression of *Tgfb1* in murine mesothelioma cell lines AB22 and AB1, showing markedly higher levels in AB1 cells, consistent with EMT activation and immunoregulatory signaling. The gene expression data for AB1 and AB22 cells were received from NCBI-GEO dataset of GSE182524 and GSE134795 respectively

Biphasic/mesenchymal mesothelioma cells display EMT-like morphology and immune evasion

The morphology and expression of EMT and immune checkpoint markers in human (MSTO-211H vs. NCI-H28) and murine (AB1 vs. AB22) mesothelioma cell lines was compared (Fig. 2). Phase-contrast imaging showed that MSTO-211H and AB1 cells displayed elongated, fibroblast-like morphologies, in contrast to the rounded, epithelial morphology observed in NCI-H28 and AB22 cells (Fig. 2 Ai, 2Aii). Quantitative analysis revealed significantly reduced circularity scores in biphasic cells ($p < 0.0001$), consistent with a more migratory, mesenchymal phenotype. Immunofluorescence staining demonstrated strong EpCAM and E-cadherin (E-Cad), a main epithelial marker expression in NCI-H28 and AB22 cells, ($p < 0.0001$ and $p = 0.0002$; Fig. 2B, 2C) while MSTO-211H and AB1 cells showed high vimentin (VIM)-a main mesenchymal marker-and PD-L1 expression, with reduced epithelial marker levels (all $p < 0.0001$; Fig. 2 B, C).

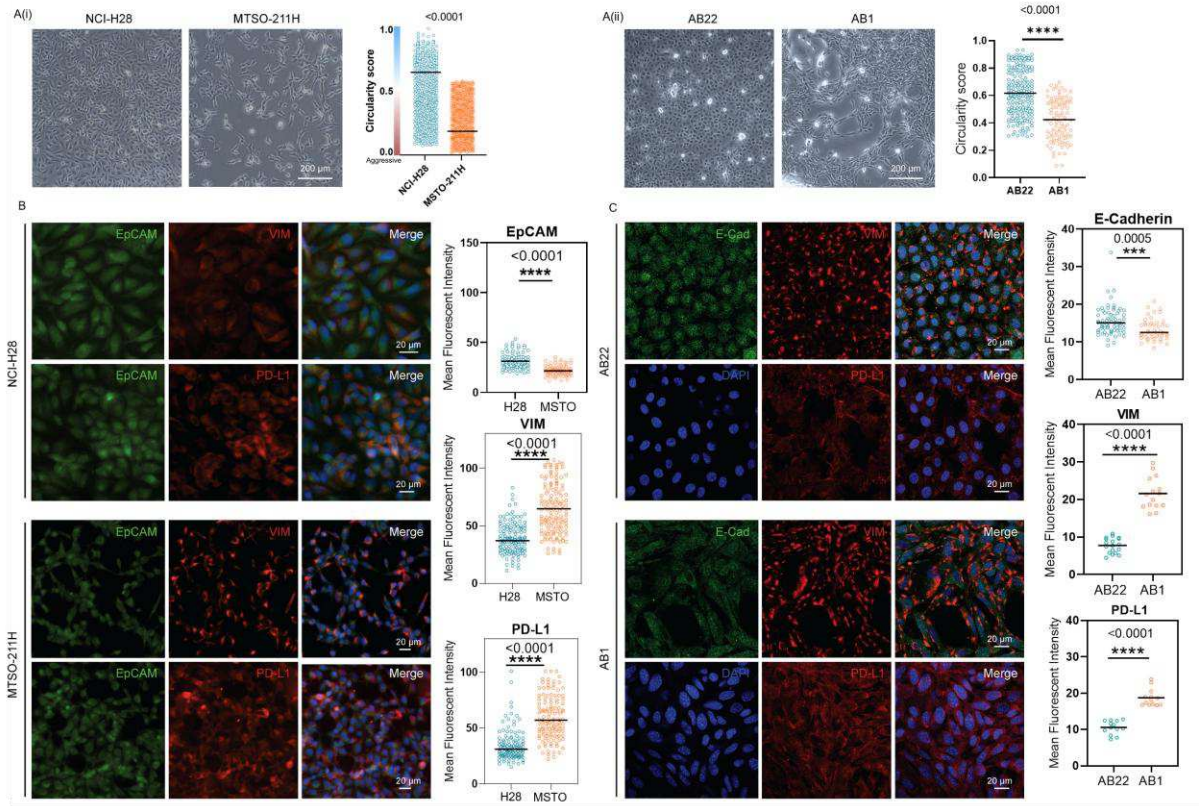


Figure-2: Morphological and molecular features distinguishing epithelial-like and mesenchymal-like mesothelioma cells. (Ai) Phase-contrast images of human mesothelioma cell lines NCI-H28 (epithelioid) and MSTO-211H (biphasic/mesenchymal-like), with quantification of cell circularity scores (n > 150 per group). NCI-H28 exhibited higher circularity, consistent with epithelial morphology, whereas MSTO-211H displayed elongated, spindle-like features indicative of mesenchymal phenotype (**p < 0.0001). (Aii) Phase-contrast imaging of murine mesothelioma cell lines AB22 (epithelioid) and AB1 (biphasic/mesenchymal-like) with corresponding circularity quantification, confirming epithelial-like morphology in AB22 and mesenchymal-like morphology in AB1 (***p < 0.0001). (B) Immunofluorescence staining of human mesothelioma cell lines for EpCAM (green), vimentin (VIM, red), and PD-L1 (magenta), with DAPI nuclear staining (blue). EpCAM expression was elevated in NCI-H28, whereas MSTO-211H showed higher VIM and PD-L1 expression. Quantification of mean fluorescent intensity (MFI) confirmed significant marker differences (****p < 0.0001). (C) Immunofluorescence analysis of murine cell lines AB22 and AB1 for E-cadherin (green), VIM (red), PD-L1 (red), and DAPI (blue) for nucleus staining. AB22 demonstrated epithelial marker expression, while AB1 was enriched for mesenchymal and immune checkpoint markers. MFI quantification revealed significantly higher VIM and PD-L1 and reduced E-cadherin in AB1 compared to AB22. Scale bars = 5 µm. *p < 0.05, **p < 0.01, ***p < 0.001, ****p < 0.0001.

sEVs from biphasic/mesenchymal Mesothelioma Cells transformed epithelial cells toward EMT-like Remodelling

Characterization of sEVs derived from biphasic MSTO-211H and AB1 mesothelioma cells revealed vesicles with expected morphology, size and protein markers (Fig. 3 A, B). The size distributions obtained by NTA showed peaks at 141 ± 64 nm for MSTO-211H-derived sEVs (Fig. 3Ai) and 112.3 ± 56.2 nm for AB1 sEVs (Fig. 3Bi), with the majority of particles measuring 100–200 nm; concentrations reached 2.7 × 10^9 particles/ml and 1.5 × 10^{10} particles/ml, respectively. Cryo-EM confirmed the expected cup-shaped morphology (Fig. 3Ai,

Bi), and Western blotting verified the presence of canonical tetraspanins CD63, CD81 and CD9 in sEVs from both cell lines (Fig. 3Aii, Bii). PD-L1 protein was detected in both MSTO-211H– and AB1-derived sEVs, indicating vesicular loading of this immune checkpoint molecule (Fig. 3Aii, Bii). Uptake of sEVs into recipient cells was confirmed by the progressive accumulation of intracellular green fluorescence, with minimal internalization at 4 hours (Fig. 3 Ci), substantial uptake by 6 hours (Fig. 3Cii) and marked intracellular vesicle accumulation by 24 hours (Fig. 3 Ciii, Supplementary video 1). To test functional mechanism, epithelial-like human NCI-H28 and murine AB22 mesothelioma cell lines were treated with MSTO-211H– and AB1-derived sEVs, respectively (Fig. 3 D, E). Compared with untreated controls, NCI-H28 cells exhibited a significant reduction in circularity (median 0.91 → 0.73; $p < 0.0001$), consistent with elongation and EMT-like morphological remodelling, a phenotype comparable to that induced by a commercial EMT reagent. Similarly, AB22 cells showed a reduction in circularity from 0.89 to 0.68 following treatment with AB1 sEVs ($p < 0.0001$), demonstrating conserved sEV-driven EMT-like transitions across species. These data indicate that biphasic/mesenchymal sEVs have the capability to trigger EMT-like changes in epithelial mesothelioma cells. Cytokine array profiling showed decreased IL-8 and CCL2 in MSTO-211H sEVs relative to parental cells (Fig. 3 F and G), while TGF-β1 was markedly enriched in MSTO-derived sEVs ($p < 0.0001$; Fig. 3 F and G). Cross checking with TCGA mesothelioma samples, TGFβ1 expression correlated positively with biphasic/mesenchymal gene signatures ($r = 0.51$; Fig. 3 H) and expression of EMT genes including TGFβ1 positively associated with expression of well-known immune-suppressive genes including IDO1, BTLA, TIGIT, TGFBR1, CD274 and CTLA4 (Fig. 3 I). In NCI-H28 cells, MSTO-derived sEVs increased SMAD2/3 phosphorylation within 4 h, whereas conditioned medium depleted of sEVs induced only a modest rise (Fig. 3 J). Following 48 h of treatment, MSTO sEVs elevated extracellular TGF-β levels, while sEV-depleted conditioned medium produced an even greater increase (Fig. 3 K). These findings indicate that biphasic mesothelioma–derived sEVs deliver TGF-β–associated signals that activate SMAD2/3 and promote EMT-related and immune-modulatory pathways in recipient cells, acting partly through localized or vesicle-associated signalling mechanisms (Fig. 3 K, L).

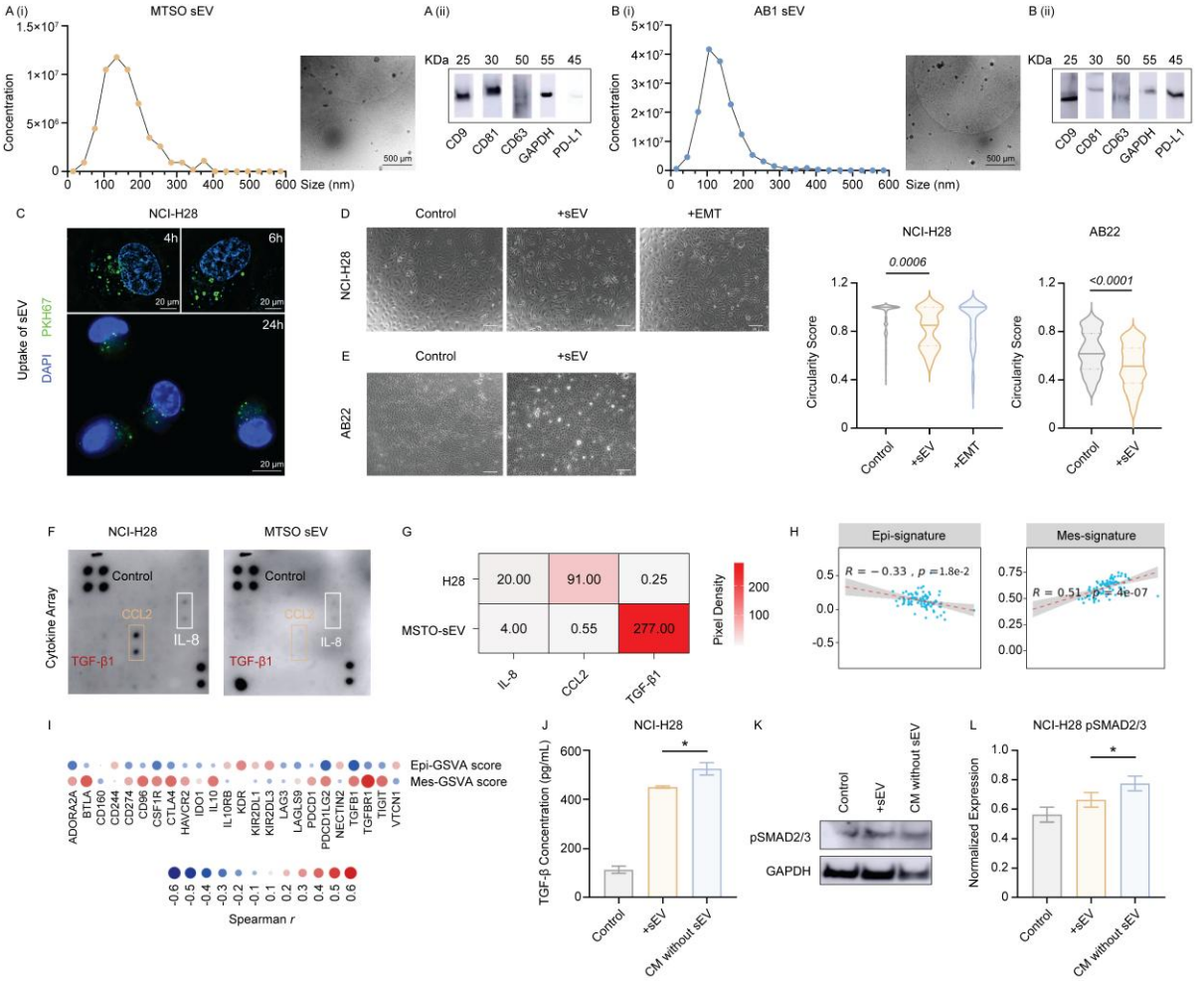


Figure-3: sEV characterization and induction of mesenchymal and immune-suppressive phenotypes. (A) Characterization of human MSTO-211H–derived sEVs by (i) nanoparticle tracking analysis (NTA) with representative cryo-EM image and (ii) Western blotting of common sEV markers (CD9, CD81, CD63), GAPDH, and PD-L1. (B) Characterization of murine AB1-derived sEVs by (i) NTA with cryo-EM and (ii) Western blotting for CD9, CD81, CD63, GAPDH, and PD-L1. (C) Uptake of PKH67-labeled sEVs (green) by NCI-H28 cells at 4 h (i), 6 h (ii), and 24 h (iii); nuclei counterstained with DAPI (blue). (D) Morphological changes and circularity score quantification in NCI-H28 cells treated with MSTO-sEVs or EMT-induction cocktail, demonstrating mesenchymal-like transition (**p = 0.0006). (E) Morphological changes and circularity score quantification in AB22 cells following AB1-sEV treatment (****p < 0.0001). (F) Cytokine array profiling of H28 cells and MSTO derived sEVs, showing increased TGF-β1 release by sEVs. (G) Quantitative cytokine heatmap confirming elevated TGF-β1 treatment (compared to H28). (H) Correlation analysis between TGF-β1 expression and epithelial (Epi) or mesenchymal (Mes) gene signatures, demonstrating inverse correlation with epithelial (R = –0.33, p = 0.0018) and positive correlation with mesenchymal scores (R = 0.51, p = 1.4e–07). (I) Correlation matrix of immune-suppressive cytokines and immune checkpoint genes with epithelial and mesenchymal GSVA scores, highlighting alignment of mesenchymal programs with immune-suppressive signalling. (I) Correlation matrix of immune-suppressive cytokines and immune checkpoint genes with epithelial and mesenchymal GSVA scores, highlighting alignment of mesenchymal programs with immune-suppressive signaling. (J) Quantification of extracellular TGF-β in NCI-H28 conditioned media following 48 h treatment with MSTO-derived sEVs, MSTO-conditioned medium depleted of sEVs. sEV treatment significantly increased extracellular TGF-β relative to untreated controls,

and sEV-depleted CM induced the highest levels. Data are Mean ± s.e.m.; n = 2 biological replicates. (K) Western blot analysis of phospho-SMAD2/3 in NCI-H28 cells 4 h after treatment with MSTO-derived sEVs or CM depleted of sEVs. Both treatments increased SMAD2/3 phosphorylation relative to controls, with sEV-depleted CM producing the strongest activation. (L) Quantification of SMAD2/3 phosphorylation corresponding to immunoblots shown in (K). MSTO-derived sEVs significantly increased phospho-SMAD2/3 levels compared with untreated controls, and sEV-depleted CM induced the highest phospho-SMAD2/3 levels. Data are Mean ± s.e.m.; n = 3 independent experiments. Scale bars = 200 nm (cryo-EM), 20 μm (immunofluorescence, morphology). *$p < 0.05$, **$p < 0.01$, ***$p < 0.001$, ****$p < 0.0001$.

Biphasic/mesenchymal cell derived sEVs induce aggressive nature in epithelial PM cells via promoting PD-L1 and vimentin expression, migration and growth

NCI-H28 epithelial cells treated with MSTO-211H-derived sEVs, showed increased PD-L1 expression by ELISA and EMT induction kit ($p < 0.0001$, one-way ANOVA; Fig. 4A) when compared to untreated cells. In migration assays, NCI-H28 cells treated with MSTO-211H-derived sEVs exhibited significantly higher migration ability by increased distance of travelled compared to all other groups ($p = 0.0001$; Fig. 4B, Supplementary video 2). This included an increase over cells treated with MSTO-211H conditioned medium depleted of sEVs, the EMT induction kit, and untreated controls (Fig. 4B). Notably, the MSTO-conditioned medium without sEVs failed to induce a comparable effect ($p > 0.05$ vs control) (Fig. 4B), indicating that soluble factors alone are insufficient to drive this pro-migratory phenotype. Additionally, while the EMT kit induced a moderate increase in migration relative to the control ($p < 0.05$), it was significantly less effective than the MSTO-derived sEV treatment ($p = 0.0001$). Proliferation increased in a concentration-dependent manner with MSTO-derived sEVs, reaching ~200% at higher concentrations (0.25μg to 1 μg; $p < 0.001$), whereas sEV-depleted conditioned medium produced only modest effects and remained significantly lower at the highest concentration ($p < 0.0001$) (Fig. 4C). Immunoblotting confirmed increased PD-L1 and VIM in NCI-H28 after MSTO-derived sEV treatment (Fig. 4D). To test whether these effects were conserved across species, we extended the analysis to a murine mesothelioma model. AB22 epithelial cells treated with biphasic/mesenchymal AB1-derived sEVs, similar with the human PM cells, this treatment induced upregulation of both PD-L1 and vimentin, as confirmed by Western blot analysis (Fig. 4 D). These findings place biphasic mesothelioma–derived sEVs upstream of coordinated EMT-associated remodelling, enhanced motility and proliferation, and induction of immune checkpoint signalling in epithelial PM cells across species.

MSTO-211H derived sEV modulate cell-cycle distribution and induce EMT/checkpoint reprogramming

There is substantial evidence in the literature linking EMT with alterations in cell cycle, particularly an enrichment of cells in the G0/G1 phase. We tested in our model, and cell cycle analysis results revealed that a higher proportion of epithelial NCI-H28 cells were arrested or enriched in the G0/G1 phase following treatment with MSTO-211H-derived sEVs compared to untreated H28 control cells (51.09% vs. 46.60%) (Fig. 4E). This shift in cell cycle distribution suggests a transition toward a quiescent or pre-proliferative state, which is characteristic of cells undergoing EMT and preparing for migratory or invasive behaviour. Consistent with this finding, treatment of NCI-H28 cells with a commercially available EMT induction kit also led to a marked enrichment of cells in the G0/G1 phase (46.20%), further supporting the association between EMT activation and cell cycle modulation. These cell-cycle

changes proof biphasic/mesenchymal -derived sEV transformed epithelial counterpart to EMT-associated reprogramming (Fig. 4E). The results of immunofluorescence staining of human NCI-H28 and murine AB22 epithelial cell lines for EMT and immune checkpoint markers with and without biphasic/mesenchymal derived sEV treatment revealed marked increase in vimentin and PD-L1 expression, accompanied by a significant reduction in E-cadherin in epithelial NCI-H28 cells (Fig. 4F), Quantification of fluorescence intensity confirmed a significant upregulation of vimentin ($p < 0.0001$), PD-L1 ($p < 0.0001$), and a significant decrease in E-cadherin ($p < 0.0001$) after sEV exposure (Fig. 4F, top right). These changes reflect a transition from an epithelial to mesenchymal state and the simultaneous activation of immune suppressive signalling. Similar effects were observed in murine AB22 cells treated with AB1-derived sEVs. Vimentin and PD-L1 levels were significantly elevated following treatment ($p < 0.0001$ for both), while E-cadherin expression was significantly decreased ($p = 0.0147$) (Fig. 4F). These consistent cross-species findings demonstrate the capacity of biphasic sEVs to induce both EMT and PD-L1 expression in epithelial mesothelioma cells.

Biphasic/mesenchymal mesothelioma–derived sEVs drive epithelial tumour reprogramming

Proteomic profiling revealed that the most defining features of MSTO-211H cells exhibiting a mesenchymal, EMT-activated tumour state and their sEVs were captured in the differential protein signatures shown in Fig. 4G–H. The volcano analysis of MSTO-211H versus NCI-H28-derived sEVs (Fig. 4G) identified a concentrated set of EMT- and immune-modulatory factors—including ANXA4, MYL6, ARF1, ARF3 and THBS1—selectively enriched in MSTO-211H derived sEVs, pinpointing the vesicular cargo most likely to transmit mesenchymal identity and to potentiate PD-L1–linked immunosuppressive signalling in epithelial recipients. The corresponding comparison of the parental cellular proteomes (Fig. 4H) demonstrated that MSTO-211H cells themselves are characterised by elevated cytoskeletal regulators, vesicle-biogenesis machinery and stress-adaptive proteins (e.g., FASN, MARCKS, PFN2, HSPA8), defining a mesenchymal, proteostasis-dependent phenotype that favours high vesicular output and EMT-competent signalling. These core observations are supported by pathway-level analyses for sEV-focused clustering and GSEA (Fig. S1A–C) that highlighted enrichment of stress-response, cell-cycle and AU-rich element–mediated post-transcriptional modules, while cellular GSEA and GO:BP analyses (Fig. S2A–C) revealed activation of proteostasis networks and TGF-β, WNT/PCP and NRF2-linked pathways in MSTO-211H—contrasting with chromatin-stabilising and metabolically structured programs in NCI-H28. By integrating these cellular (Fig. 4H) and vesicular (Fig. 4G) landscapes, the data demonstrate that EMT-driven reprogramming in MSTO-211H cells governs selective loading of immune-modulatory and EMT-enhancing cargo into sEVs, providing the mechanistic basis by which biphasic mesothelioma sEVs potentiate EMT progression and reinforce PD-L1–mediated T-cell suppression—central to the aim of this study.

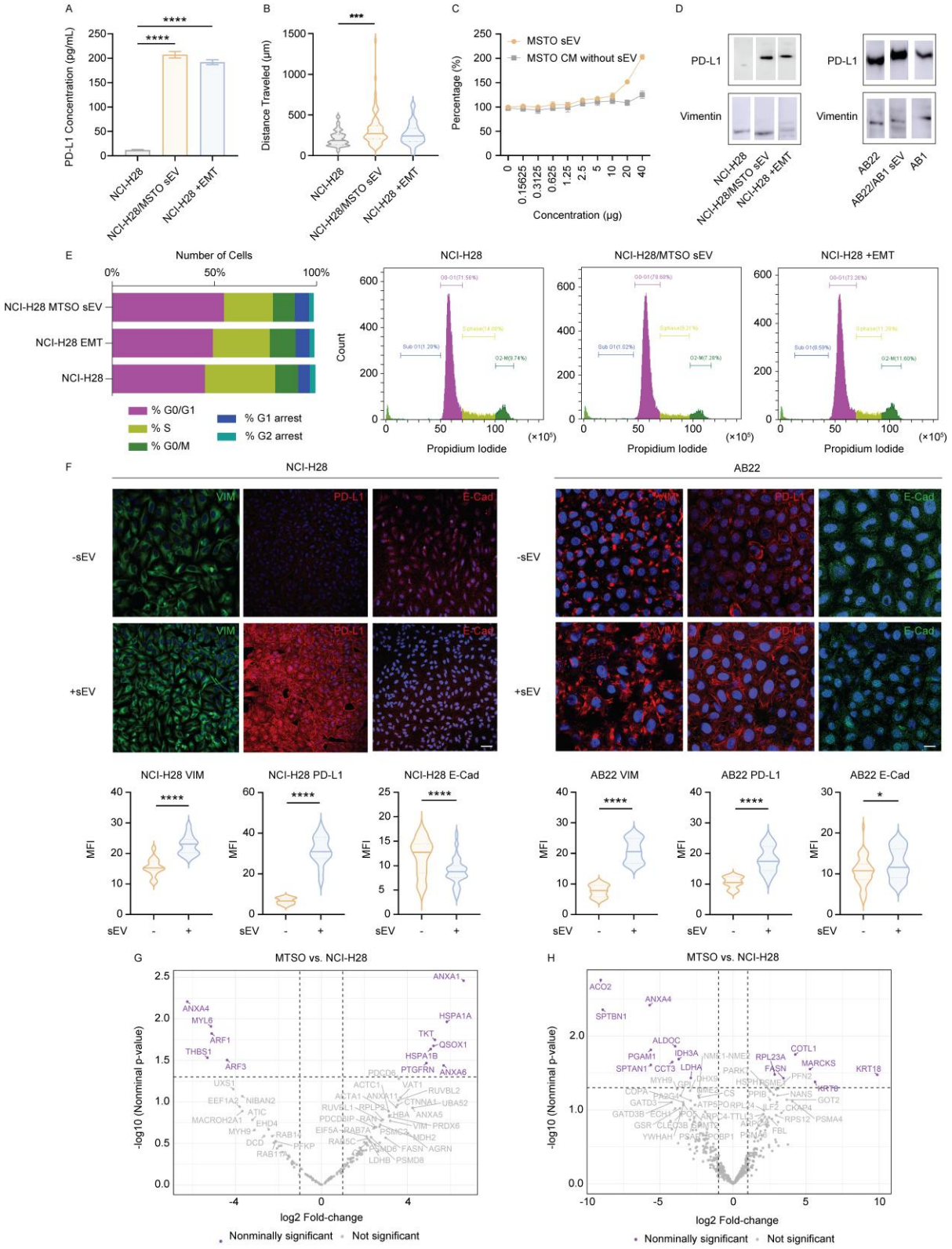


Figure-4: MSTO- and AB1-derived sEVs elevate PD-L1, promote EMT features, migration, and growth in epithelioid mesothelioma cells. (A) ELISA of PD-L1 in NCI-H28 cells: untreated control, MSTO-sEV–treated, and EMT-induction kit (positive control). MSTO-sEVs significantly increased PD-L1 (***$p < 0.0001$), comparable to control and EMT induction. (B) Migration assay (total distance travelled, μm) showing enhanced motility of NCI-H28 after MSTO-sEV treatment relative to control, with EMT induction as a positive control (***$p < 0.0001$). (C) Proliferation/viability across a serial 1:2 dilution of MSTO-sEVs (0.15–40 μg),

benchmarked against MSTO conditioned medium without sEVs; responses are expressed as % of untreated controls (mean ± SD; n=3 independent experiments). (D) Western blots for PD-L1 and Vimentin in human (H28 ± MSTO-sEV; H28 ± EMT kit) and murine (AB22 ± AB1-sEV; AB1) cells, confirming induction of immune-evasion (PD-L1) and mesenchymal (VIM) markers following sEV or EMT treatment. (E) Cell-cycle profiling (PI) of NCI-H28 cells (control, EMT, MSTO-sEV) showing altered phase distribution (stacked bars and representative histograms). (F) Immunofluorescence of Vimentin (VIM), PD-L1, and E-cadherin (E-Cad) with DAPI (blue) in NCI-H28 (± MSTO-sEV) and AB22 (± AB1-sEV). Quantified mean fluorescent intensity (MFI) demonstrates increased VIM and PD-L1 and reduced E-Cad in sEV-treated cells (H28: ****$p < 0.0001$; AB22: VIM/PD-L1 ****$p < 0.0001$, E-Cad *$p < 0.05$). Scale bars, 5 μm. Significance: *$p < 0.05$, **$p < 0.01$, ***$p < 0.001$, ***$p < 0.0001$. Proteomic profiling and functional enrichment analysis of H28 and MSTO derived sEVs. (G) Volcano plot displaying differentially abundant proteins between MSTO- and H28-derived SEVs. Notably, ANXA4, MYL9, ARF1, ARF3, and THBS1 emerge as significantly upregulated in MSTO-SEVs, implicating these proteins as potential effectors of immune checkpoint activation and EMT induction in recipient H28 cells. (H) Volcano plot comparing MSTO versus H28 proteomes identifies significantly altered proteins, including ANXA4, LDHA, PGAM1, FASN, COL11, and KRT18, many of which are associated with metabolic rewiring and EMT.

AB1-derived sEVs reshape tumour-immune interactions in 3D and 2D co-cultures

To assess the impact of tumour-derived sEVs on tumour–immune interactions in a 3D context, AB22 cells and activated murine T cells were embedded in a collagen–PIC hydrogel matrix and treated with AB1-derived sEVs. Prespecified endpoints included $CD4^+$ and $CD8^+$ T-cell density, tumour PD-L1 expression and Ki-67 positivity (Fig. 5). Across biologically independent experiments, AB1-sEV treatment resulted in a marked reduction of $CD8^+$ T-cell abundance relative to PBS controls (two-sided tests, $P < 1\times10^{-5}$; Fig. 5 A, B). In parallel, PD-L1 expression in AB22 tumour cells increased following sEV treatment ($P < 1\times10^{-5}$; Fig. 5 A, B), consistent with sEV-mediated immune modulation coupled to EMT. To assess proliferative consequences, Ki-67 was quantified by immunofluorescence and higher Ki-67 positivity observed after treating epithelial AB22 cells to AB1–derived sEVs compared to untreated controls ($P = 1\times10^{-4}$; Fig. 5 A, B). In the same 3D co-cultures, total $CD4^+$ T-cell abundance was maintained or modestly increased following AB1 sEV treatment, resulting in an elevated CD4:CD8 ratio relative to PBS controls (Fig. 5 A, B).

Histopathological analysis of AB22 co-cultures with activated T cells sourced from mice splenocytes revealed disruption of tumour architecture, with loss of cohesion, irregular cell shapes and infiltration by small, round, basophilic cells consistent with lymphocytes (Fig. 5 C). Nuclear condensation, fragmentation, cytoplasmic shrinkage and eosinophilic debris were evident, consistent with apoptotic cell death. Co-cultures treated with AB1-derived sEVs displayed more pronounced disruption of tumour architecture, increased immune-cell infiltration at the tumour periphery and within tumour clusters, and more pronounced apoptotic features compared with co-cultures without biphasic/mesenchymal AB1-derived sEVs (Fig. 5 C).

Cytokine profiling of AB22–splenocyte co-cultures demonstrated that AB1-derived sEVs reshaped the secretome toward a pro-inflammatory and myeloid-activating profile. IL-1F and IL-5 were prominently increased following sEV treatment (from ~195–200 AU to >210–220 AU; Fig. 5 D). Notably, M-CSF, a key driver of monocyte-to-macrophage differentiation, was also consistently elevated in the sEV-treated group, indicative of active recruitment and polarization of myeloid cells within the tumour–immune microenvironment. Interestingly,

CCL17, a canonical CCR4 ligand associated with Treg and Th2 chemotaxis, displayed a divergent response, suggesting that sEVs may selectively promote inflammatory rather than immunosuppressive chemokine responses in this context (Fig. 5 D). In a complementary 2D co-culture system, flow cytometric analysis revealed that, in the absence of sEVs, $CD8^+$ and $CD4^+$ T cells represented 31.3% and 34.9% of events, respectively (Fig. 5 E). Following treatment with 10 µg AB1-derived sEVs for 48 hours, the total T-cell population decreased to 3.77% of events, with $CD8^+$ T cells reduced to 0.33% and $CD4^+$ T cells to 1.63% ($p = 0.001$; Fig. 5 E). Across 3D and 2D systems, AB1-derived sEVs consistently altered tumour–immune dynamics by reducing cytotoxic T-cell representation, increasing tumour PD-L1 expression and proliferation, and reshaping immune infiltration and cytokine output, establishing sEV-mediated communication as a central determinant of mesothelioma immune remodelling (Fig. 5).

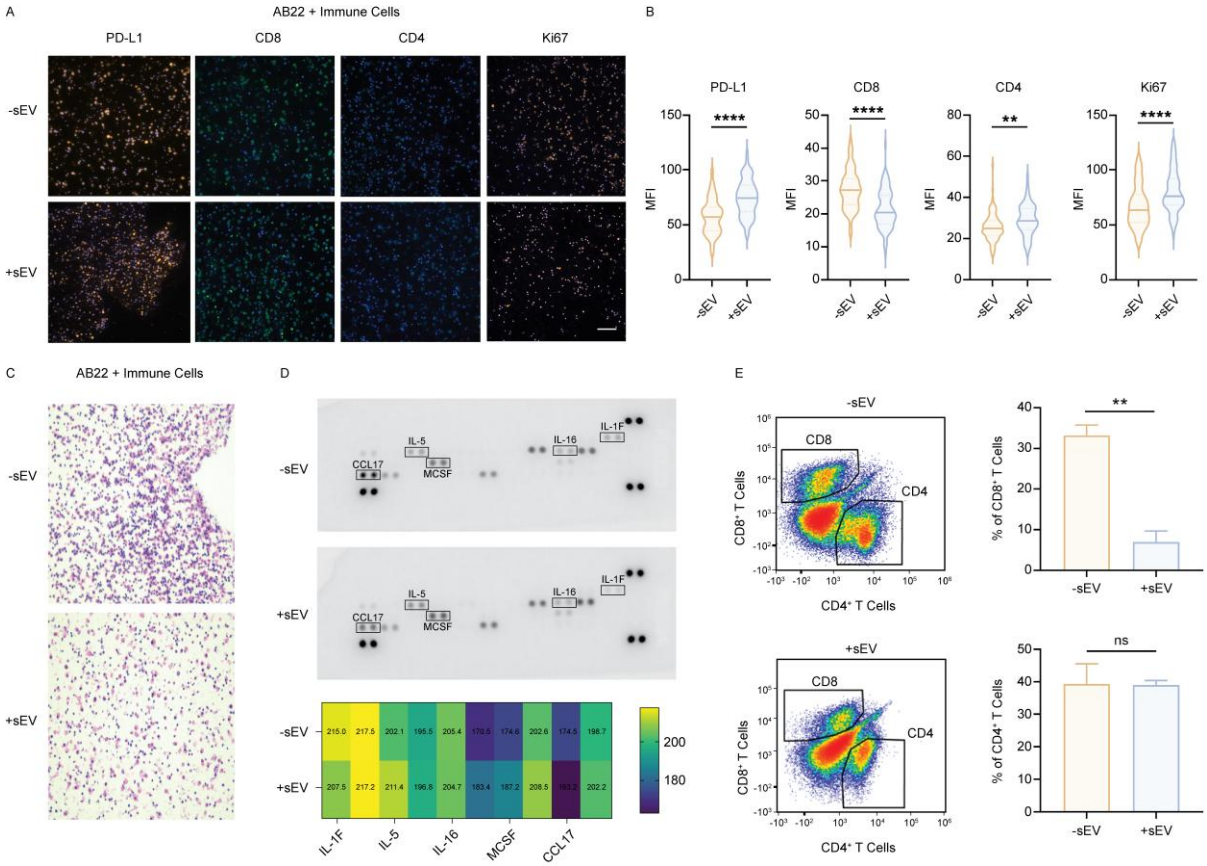


Figure-5: Immune modulation by mesothelioma-derived sEVs in co-culture models. (A) Representative immunofluorescence staining of AB22 cells co-cultured with immune cells, with and without AB1-sEV treatment, showing PD-L1, CD8, CD4, and Ki67 expression. Scale bars = 5 µm. (B) Quantification of MFI revealed significantly increased PD-L1 and Ki67 expression, together with altered CD8 and CD4 expression in sEV-treated samples compared to untreated controls (***$p < 0.0001$, **$p < 0.01$). (C) H&E staining of AB22 cells co-cultured with immune cells, comparing untreated and AB1-sEV–treated conditions. (D) Cytokine array analysis of AB22 co-cultures with and without AB1-sEVs showing altered cytokine secretion patterns, including IL-1F, IL-5, IL-16, M-CSF, and CCL17. The heatmap summarizes relative cytokine expression intensities. (E) Flow cytometry analysis of CD8+ and CD4+ T-cell populations from co-culture assays. tSNE plots highlight clustering and proportions of CD8+ and CD4+ T cells. Quantification confirmed a significant reduction in CD8+ T cells after AB1-sEV treatment (**$p < 0.01$), while CD4+ populations remained unchanged (ns). Data indicates that sEV treatment enhances PD-L1 and Ki67 expression in tumour cells, suppresses CD8+ T-

cell activity, alters cytokine signalling, and promotes an immunosuppressive microenvironment.

Discussion

This study identifies EMT as a key organiser of tumour plasticity in mesothelioma and shows that EMT actively reshapes the composition and function of tumour-derived sEVs. By linking EMT to both phenotypic reprogramming and immune suppression, these findings position EMT as a driver of tumour evolution within the pleural microenvironment. Although sEVs have been implicated in immune activity rewiring in several tumour types [40,41], their functional contribution to EMT-linked immunosuppression in mesothelioma remained unresolved. Our data reveal that EMT enhances PD-L1 loading into sEVs, generating a vesicle population with direct T-cell–suppressive activity, addressing a previously undefined mechanism in this cancer.

While PD-L1 transport via sEVs has been described in other malignancies [28 42], the present study clarifies its positioning within mesothelioma biology by demonstrating that EMT acts upstream of PD-L1 vesicular loading. This establishes a mechanistic route by which mesenchymal reprogramming potentiates immune evasion.

Our findings extend these observations by showing that mesothelioma sEVs deliver a coordinated EMT-associated protein programme rather than isolated transcriptional regulators. This supports a model in which aggressive tumour subpopulations can horizontally disseminate mesenchymal traits to less invasive cells.

The stated depletion of $CD4^+$ and $CD8^+$ T cells induced by PD-L1–high sEVs aligns with the potent immunosuppressive properties of vesicular PD-L1 observed in other cancers [43 44-46], while establishing its direct functional relevance in mesothelioma. Consistent with these broader themes, our results indicate that EMT enhances the release of vesicles capable of reprogramming tumour cells and suppressing immune effectors, defining an EMT-sEV axis that integrates tumour plasticity with immune escape.

Proteomic analysis revealed an EMT-associated vesicle signature unique to mesothelioma, including FASN, MARCKS, ANXA4, PFN2 and HSPA8. These proteins are linked to lipid metabolic rewiring [47 48], actin cytoskeletal dynamics [49] and stress-adaptive signalling [50 51], processes integral to EMT and invasive behaviour. Their transfer to NCI-H28 cells provides a mechanistic explanation for the acquisition of mesenchymal traits following exposure to MSTO-211H derived sEVs. In contrast, NCI-H28-derived and normal sEVs were enriched for keratins (KRT5, KRT6, KRT10), consistent with a more epithelial identity. This divergence highlights sEVs as conveyors of tumour state, exporting differentiation-specific information that shapes the behaviour of neighbouring cells.

The polarity in vesicle cargo composition indicates that MSTO-211H derived sEVs preferentially export proteins aligned with mesenchymal and stress-adaptive states, whereas NCI-H28-derived sEVs retain components characteristic of a more epithelial phenotype. These vesicle profiles parallel the phenotypic differences observed between parental cells and suggest a selective mechanism of protein packaging linked to EMT status. Comparison of cellular and vesicular proteomes showed that MSTO-211H cells preferentially expressed proteins involved in cytoskeletal organization and vesicle biogenesis, such as FASN, MARCKS and PFN2 features echoed in their sEV cargo. This alignment supports a model in which mesenchymal-state cells export functional components that reinforce invasive and plastic behaviours. In contrast, NCI-H28 cells showed stronger expression of keratins (KRT8/18) and metabolic enzymes including ALDOC, PGAM1 and LDHA, and these proteins were correspondingly represented in NCI-H28-derived sEVs. The overlap between cellular and vesicular proteomes

indicates that vesicles from epithelial-like cells primarily reflect a metabolically active, less mesenchymal state. Direct comparison across compartments confirms that sEV cargo is a curated subset of parental cell proteomes. MSTO-211H derived sEVs are biased toward EMT- and immune-modulatory proteins (ANXA4, MYL6, THBS1), whereas NCI-H28-derived sEVs favour epithelial markers, consistent with the profiles observed in the volcano plots. These patterns indicate that EMT status shapes sEV cargo composition in ways that may influence paracrine signalling and tumour–immune interactions.

Our findings provide the first direct demonstration in mesothelioma that PD-L1–rich sEVs suppress both $CD4^+$ and $CD8^+$ T-cell populations, which are similar with mechanisms reported in glioblastoma, [50] HNSCC, [33] melanoma, gastric [51] and oral cancers. [35] The selective loss of T-cell subsets, together with the presence of TGF-β within tumour sEVs [31,52] suggests coordinated immunomodulatory signalling capable of driving T-cell apoptosis, dysfunction or exhaustion. These observations establish vesicle-associated PD-L1 as a dominant immunosuppressive mechanism in mesothelioma and reveal how EMT-enhanced vesicle output contributes to shaping an immune-permissive tumour ecosystem.

This work defines a mechanistic framework in which EMT reconfigures sEV biogenesis and cargo selection to propagate mesenchymal traits while simultaneously suppressing antitumour immunity. By coupling phenotypic plasticity with PD-L1–mediated immune suppression, EMT-dependent sEV signalling emerges as a central regulator of mesothelioma progression and immune escape. This EMT–sEV axis positions vesicle biology as an active driver of tumour evolution and highlights EMT-associated vesicle cargo as a potential target for minimally-invasive liquid biopsy diagnosis and therapeutic intervention.

Conclusion

This study identifies a previously unrecognized mechanism of immune evasion in pleural mesothelioma driven by sEVs released from mesenchymal-like tumour cells. These sEVs induce EMT in epithelial PM cells, reflected by decreased E-cadherin, increased vimentin, and pronounced morphological and functional changes. In parallel, they exhibit markedly elevated PD-L1, enabling potent suppression of $CD8^+$ T-cell proliferation, frequency, and infiltration across both 2D and physiologically relevant 3D tumour–immune co-culture systems. The combined ability of biphasic/mesenchymal cell derived sEVs to reprogramme tumour phenotype while attenuating cytotoxic immunity positions them as central orchestrators of immune resistance in PM. These effects in human and murine models further supports a cross-species mechanism of sEV-mediated immunomodulation. These findings establish sEV-associated EMT and PD-L1 signalling as actionable drivers of tumour progression and highlight tumour-derived sEVs as promising therapeutic targets for overcoming immunotherapy resistance in pleural mesothelioma.

Fellowship Program (PRO22-15457) and National Health Medical Research Council (2025442). No other specific grant from public, commercial or not-for-profit funding agencies was received for this study.

List of abbreviations

PM	Pleural mesothelioma
sEV	Small extracellular Vesicles
EMT	epithelial-to-mesenchymal transition

TGF-β1	Transforming Growth Factor Beta 1
PD-L1	Programmed Death-Ligand 1
$CD8^+$	Cluster of Differentiation 8 = cytotoxic T cell
CDH1	Cadherin-1
EpCAM	Epithelial Cell Adhesion Molecule
$CD4^+$	Cluster of Differentiation 4 = helper T cells
SNAREs	Soluble NSF Attachment Protein Receptors
Alix	ALG-2–interacting protein X
TSG101	tumour susceptibility gene 101
MHC1	major histocompatibility complex 1
HSP90	heat shock protein 90
β-catenin	Beta-catenin
HIF-1α	Hypoxia-Inducible Factor 1-alpha
PFA	paraformaldehyde
CM	conditioned medium
SDS–PAGE	Sodium Dodecyl Sulfate–Polyacrylamide Gel Electrophoresis
PVDF	Polyvinylidene fluoride (PVDF) membrane
ELISA	Enzyme-Linked Immunosorbent Assay
SMAD2/3	SMAD Family Member 2 and SMAD Family Member 3
IL-2	interleukin-2
PerCP-Cy5.5	PerCP-Cy5.5 (peridinin chlorophyll protein–Cy5.5)
DAPI	4′,6-diamidino-2-phenylindole
H&E	Hematoxylin and Eosin
LC–MS/MS	Liquid Chromatography–Tandem Mass Spectrometry
TCGA	The Cancer Genome Atlas
TME	Tumor Microenvironment
FOXP3	Forkhead Box P3
GSVA	Gene set variation analysis
MFI	Quantified mean fluorescent intensity
PIC	Polyisocyanopeptide

Declarations

Ethics Approval Statement

All procedures involving the isolation of splenocytes from BALB/c mice were conducted in accordance with the National Health and Medical Research Council Australian Code for the Care and Use of Animals for Scientific Purposes. Mouse spleens used in this study were obtained as incidental biological material from animals that were routinely culled, and are therefore classified as waste tissue. As such, no specific animal ethics approval number was required for their use.

Consent for publication

Not Applicable

Availability of data and materials

Publicly available data from The Cancer Genome Atlas mesothelioma cohort (TCGA-MESO) were used in this study and can be accessed through the TCGA data portal. All other datasets generated and analysed during the current study (including proteomic, transcriptomic, imaging and cytokine profiling data from MSTO-211H, NCI-H28, AB1 and AB22 cell lines and associated sEV preparations are available from the corresponding authors upon reasonable request.

Competing interests

The authors declare that they have no competing interests.

Funding Statement

This work was partially supported by the NSW Dust Diseases Authority (iCARE) 2023/24 Ideas to Action Grant.

Author's Contributions

YYC conceived the study, developed the experimental design, secured funding, supervised the project, and edited the manuscript. SZ performed the majority of the experiments, conducted data analysis, and drafted and revised the manuscript. HA performed TCGA data analysis. ER conducted statistical and proteomics analyses. JN, XC, and ZC assisted with key experimental procedures, including sEV isolation, splenic immune cell isolation, and cell tracking experiments. OG and EL contributed murine splenic immune cells. ME, NW, and AR designed the PIC system and optimised conditions for 3D culture. ZW contributed to figure preparation, layout, and design. DMG and JL contributed to manuscript editing. MW contributed to the initial conceptual development of the project and approved the final version of the manuscript. All authors read and approved the final manuscript.

Acknowledgments

We gratefully acknowledge the Cryo-Electron Microscopy Facility at the Victor Chang Cardiac Research Institute Innovation Centre, supported by the NSW Government, and the Electron Microscope Unit within the Mark Wainwright Analytical Centre (MWAC), UNSW Sydney. We also thank the Microscopy Imaging Facility (MIF), particularly Dr Louise Cole and Dr Amy Bottomly, for their support with imaging. We are indebted to Professor Dayong Jin (University of Technology Sydney) for valuable guidance during manuscript preparation. M.E.W. acknowledges funding from the Cancer Institute New South Wales through a DG Fellowship (2021CDF1148). JYL acknowledges funding from UTS Chancellor's Research

Permission to Reproduce Material from Other Sources

All figures, tables and datasets presented in this manuscript are original and were generated by the authors. No previously published material has been reproduced. If any third-party material is included in the final version, permission will be obtained from the copyright holders and appropriately acknowledged.

References:

1 Tsao, A. S., Wistuba, I., Roth, J. A. & Kindler, H. L. Malignant pleural mesothelioma. *J Clin Oncol* **27**, 2081–2090 (2009). https://doi.org/10.1200/jco.2008.19.8523

2 Zhang, W., Wu, X., Wu, L., Zhang, W. & Zhao, X. Advances in the diagnosis, treatment and prognosis of malignant pleural mesothelioma. *Ann Transl Med* **3**, 182 (2015). https://doi.org/10.3978/j.issn.2305-5839.2015.07.03

3 Faig, J. *et al.* Changing pattern in malignant mesothelioma survival. *Transl Oncol* **8**, 35–39 (2015). https://doi.org/10.1016/j.tranon.2014.12.002

4 Escalon, J. G. *et al.* Malignant pleural mesothelioma: are there imaging characteristics associated with different histologic subtypes on computed tomography? **42**, 601 (2018).

5 Wu, L., Amjad, S., Yun, H., Mani, S. & de Perrot, M. J. S. r. A panel of emerging EMT genes identified in malignant mesothelioma. **12**, 1–16 (2022).

6 Ramundo, V., Zanirato, G. & Aldieri, E. J. I. J. o. M. S. The Epithelial-to-Mesenchymal Transition (EMT) in the Development and Metastasis of Malignant Pleural Mesothelioma. **22**, 12216 (2021).

7 Katsuno, Y. & Derynck, R. J. D. C. Epithelial plasticity, epithelial-mesenchymal transition, and the TGF-β family. **56**, 726–746 (2021).

8 Dongre, A. & Weinberg, R. A. J. N. r. M. c. b. New insights into the mechanisms of epithelial–mesenchymal transition and implications for cancer. **20**, 69–84 (2019).

9 Pastushenko, I. & Blanpain, C. J. T. i. c. b. EMT transition states during tumor progression and metastasis. **29**, 212–226 (2019).

10 Chen, Daniel S. & Mellman, I. Oncology Meets Immunology: The Cancer-Immunity Cycle. *Immunity* **39**, 1–10 (2013). https://doi.org/https://doi.org/10.1016/j.immuni.2013.07.012

11 Lou, Y. *et al.* Epithelial–Mesenchymal Transition Is Associated with a Distinct Tumor Microenvironment Including Elevation of Inflammatory Signals and Multiple Immune Checkpoints in Lung Adenocarcinoma. *Clinical Cancer Research* **22**, 3630–3642 (2016). https://doi.org/10.1158/1078-0432.CCR-15-1434

12 Iwai, Y. *et al.* Involvement of PD-L1 on tumor cells in the escape from host immune system and tumor immunotherapy by PD-L1 blockade. *Proc Natl Acad Sci U S A* **99**, 12293–12297 (2002). https://doi.org/10.1073/pnas.192461099

13 Blank, C., Gajewski, T. F. & Mackensen, A. Interaction of PD-L1 on tumor cells with PD-1 on tumor-specific T cells as a mechanism of immune evasion: implications for tumor immunotherapy. *Cancer Immunol Immunother* **54**, 307–314 (2005). https://doi.org/10.1007/s00262-004-0593-x

14 Azuma, T. *et al.* B7-H1 is a ubiquitous antiapoptotic receptor on cancer cells. *Blood* **111**, 3635–3643 (2008). https://doi.org/10.1182/blood-2007-11-123141

15 Kim, Y. T. Local Therapy for Pulmonary Oligometastases: Is SABR a New Champion? *Journal of Thoracic Oncology* **12**, 1335–1337 (2017). https://doi.org/https://doi.org/10.1016/j.jtho.2017.07.004

16 Howell, M., Lee, R., Bowyer, S., Fusi, A. & Lorigan, P. Optimal management of immune-related toxicities associated with checkpoint inhibitors in lung cancer. *Lung Cancer* **88**, 117–123 (2015). https://doi.org/https://doi.org/10.1016/j.lungcan.2015.02.007

17 Kao, S. C. *et al.* Tumor Suppressor microRNAs Contribute to the Regulation of PD-L1 Expression in Malignant Pleural Mesothelioma. *Journal of Thoracic Oncology* **12**, 1421–1433 (2017). https://doi.org/https://doi.org/10.1016/j.jtho.2017.05.024

18 Qian, K. *et al.* The roles of small extracellular vesicles in cancer and immune regulation and translational potential in cancer therapy. *Journal of Experimental & Clinical Cancer Research* **41**, 286 (2022). https://doi.org/10.1186/s13046-022-02492-1

19 Wang, J. *et al.* Exosomal PD-L1 and N-cadherin predict pulmonary metastasis progression for osteosarcoma patients. *Journal of Nanobiotechnology* **18**, 151 (2020). https://doi.org/10.1186/s12951-020-00710-6

20 Szempruch, A. J. *et al.* Extracellular vesicles from Trypanosoma brucei mediate virulence factor transfer and cause host anemia. *Cell* **164**, 246–257 (2016).

21 Gangoda, L., Boukouris, S., Liem, M., Kalra, H. & Mathivanan, S. Extracellular vesicles including exosomes are mediators of signal transduction: are they protective or pathogenic? *Proteomics* **15**, 260–271 (2015).

22 Hoshino, A. *et al.* Tumour exosome integrins determine organotropic metastasis. *Nature* **527**, 329–335 (2015).

23 Zhang, L. *et al.* Microenvironment-induced PTEN loss by exosomal microRNA primes brain metastasis outgrowth. *Nature* **527**, 100–104 (2015).

24 Andreu, Z. & Yáñez-Mó, M. Tetraspanins in extracellular vesicle formation and function. *Front Immunol* **5**, 442 (2014). https://doi.org/10.3389/fimmu.2014.00442

25 Van Niel, G., Porto-Carreiro, I., Simoes, S. & Raposo, G. Exosomes: a common pathway for a specialized function. *Journal of biochemistry* **140**, 13–21 (2006).

26 Mulcahy, L. A., Pink, R. C. & Carter, D. R. Routes and mechanisms of extracellular vesicle uptake. *J Extracell Vesicles* **3** (2014). https://doi.org/10.3402/jev.v3.24641

27 You, Y. *et al.* Matrix metalloproteinase 13-containing exosomes promote nasopharyngeal carcinoma metastasis. *Cancer Sci* **106**, 1669–1677 (2015). https://doi.org/10.1111/cas.12818

28 Chen, G. *et al.* Exosomal PD-L1 contributes to immunosuppression and is associated with anti-PD-1 response. *Nature* **560**, 382–386 (2018). https://doi.org/10.1038/s41586-018-0392-8

29 Hood, J. L., San, R. S. & Wickline, S. A. Exosomes released by melanoma cells prepare sentinel lymph nodes for tumor metastasis. *Cancer Res* **71**, 3792–3801 (2011). https://doi.org/10.1158/0008-5472.Can-10-4455

30 Yang, Y. *et al.* Exosomal PD-L1 harbors active defense function to suppress T cell killing of breast cancer cells and promote tumor growth. *Cell Res* **28**, 862–864 (2018). https://doi.org/10.1038/s41422-018-0060-4

31 Li, C. *et al.* Clinical significance of PD-L1 expression in serum-derived exosomes in NSCLC patients. *J Transl Med* **17**, 355 (2019). https://doi.org/10.1186/s12967-019-2101-2

32 Poggio, M. *et al.* Suppression of Exosomal PD-L1 Induces Systemic Anti-tumor Immunity and Memory. *Cell* **177**, 414–427.e413 (2019). https://doi.org/10.1016/j.cell.2019.02.016

33 Theodoraki, M. N., Hoffmann, T. K., Jackson, E. K. & Whiteside, T. L. Exosomes in HNSCC plasma as surrogate markers of tumour progression and immune competence. *Clin Exp Immunol* **194**, 67–78 (2018). https://doi.org/10.1111/cei.13157

34 Theodoraki, M. N., Yerneni, S. S., Hoffmann, T. K., Gooding, W. E. & Whiteside, T. L. Clinical Significance of PD-L1(+) Exosomes in Plasma of Head and Neck Cancer Patients. *Clin Cancer Res* **24**, 896–905 (2018). https://doi.org/10.1158/1078-0432.Ccr-17-2664

35 Razzo, B. M. *et al.* Tumor-derived exosomes promote carcinogenesis of murine oral squamous cell carcinoma. *Carcinogenesis* **41**, 625–633 (2020). https://doi.org/10.1093/carcin/bgz124

36 Fan, Y. *et al.* Exosomal PD-L1 Retains Immunosuppressive Activity and is Associated with Gastric Cancer Prognosis. *Ann Surg Oncol* **26**, 3745–3755 (2019). https://doi.org/10.1245/s10434-019-07431-7

37 Zhand, S. *et al.* Small Extracellular Vesicle-Derived Circular RNA hsa_circ_0007386 as a Biomarker for the Diagnosis of Pleural Mesothelioma. *Cells* **13** (2024). https://doi.org/10.3390/cells13121037

38 Zimoch, J. *et al.* Polyisocyanopeptide hydrogels: A novel thermo-responsive hydrogel supporting pre-vascularization and the development of organotypic structures. *Acta Biomaterialia* **70**, 129–139 (2018). https://doi.org/https://doi.org/10.1016/j.actbio.2018.01.042

39 Enriquez Martinez, M. A. *et al.* Tuning collagen nonlinear mechanics with interpenetrating networks drives adaptive cellular phenotypes in three dimensions. *Sci Adv* **11**, eadt3352 (2025). https://doi.org/10.1126/sciadv.adt3352

40 Kalluri, R. & LeBleu, V. S. The biology, function, and biomedical applications of exosomes. *Science* **367**, eaau6977 (2020). https://doi.org/10.1126/science.aau6977

41 Pathania, A. S., Prathipati, P. & Challagundla, K. B. New insights into exosome mediated tumor-immune escape: Clinical perspectives and therapeutic strategies. *Biochim Biophys Acta Rev Cancer* **1876**, 188624 (2021). https://doi.org/10.1016/j.bbcan.2021.188624

42 Chen, L. *et al.* HCC-derived exosomes elicit HCC progression and recurrence by epithelial-mesenchymal transition through MAPK/ERK signalling pathway. *Cell Death Dis* **9**, 513 (2018). https://doi.org/10.1038/s41419-018-0534-9

43 Nakayama, F. *et al.* Pancreatic cancer cell-derived exosomes induce epithelial-mesenchymal transition in human pancreatic cancer cells themselves partially via transforming growth factor β1. *Medical Molecular Morphology* **55**, 227–235 (2022). https://doi.org/10.1007/s00795-022-00321-0

44 Röhrig, F. & Schulze, A. The multifaceted roles of fatty acid synthesis in cancer. *Nature Reviews Cancer* **16**, 732–749 (2016). https://doi.org/10.1038/nrc.2016.89

45 Menendez, J. A. & Lupu, R. Fatty acid synthase and the lipogenic phenotype in cancer pathogenesis. *Nature Reviews Cancer* **7**, 763–777 (2007). https://doi.org/10.1038/nrc2222

46 Menendez, J. A. *et al.* Fatty acid synthase (FASN) signalome: A molecular guide for precision oncology. *Mol Oncol* **18**, 479–516 (2024). https://doi.org/10.1002/1878-0261.13582

47 Juin, P., Geneste, O., Raimbaud, E. & Hickman, J. A. Shooting at survivors: Bcl-2 family members as drug targets for cancer. *Biochimica et Biophysica Acta (BBA) - Molecular Cell Research* **1644**, 251–260 (2004). https://doi.org/https://doi.org/10.1016/j.bbamcr.2003.10.010

48 Sokolova, O. & Naumann, M. NF-κB Signaling in Gastric Cancer. *Toxins (Basel)* **9** (2017). https://doi.org/10.3390/toxins9040119

49 Liu, S. *et al.* Serum exosomal proteomics analysis of lung adenocarcinoma to discover new tumor markers. *BMC Cancer* **22**, 279 (2022). https://doi.org/10.1186/s12885-022-09366-x

50 Ricklefs, F. L. *et al.* Immune evasion mediated by PD-L1 on glioblastoma-derived extracellular vesicles. *Sci Adv* **4**, eaar2766 (2018). https://doi.org/10.1126/sciadv.aar2766

51 Cordonnier, M. *et al.* Tracking the evolution of circulating exosomal-PD-L1 to monitor melanoma patients. *J Extracell Vesicles* **9**, 1710899 (2020). https://doi.org/10.1080/20013078.2019.1710899

52 Huang, S. H., Li, Y., Zhang, J., Rong, J. & Ye, S. Epidermal growth factor receptor-containing exosomes induce tumor-specific regulatory T cells. *Cancer Invest* **31**, 330–335 (2013). https://doi.org/10.3109/07357907.2013.789905

Supplementary Files

This is a list of supplementary files associated with this preprint. Click to download.

- Supplementary04022026.docx
- Supplimentaryfulluncropedwesternimages.pdf